AGL: A UWB Technology for Precise Positioning and Navigation in the Edge Spaces

Muhammad Hafeez Chaudhary*, Bart Scheers

Royal Military Academy, 30 Avenue de la Renaissance, 1000 Brussels, Belgium

Abstract

This paper introduces the Agilica Geo-Location (AGL) system, an Ultra-wideband (UWB) technology-based solution designed for precise positioning and tracking in challenging edge spaces. In these environments, traditional Global Navigation Satellite System (GNSS) coverage is often obstructed or unavailable, leading to inadequate positioning accuracy. Such scenarios are critical, especially for applications like autonomous drone landing on sea vessels, where onboard structures can obstruct a large part of the sky during the landing phase. Unlike many other UWB-based solutions, AGL supports both *network-centric* asset tracking and *device-centric* navigation simultaneously, enabling scalability and adaptability. The system's auto-calibration mechanism and robust signal processing ensure reliable performance even in challenging RF channel environments. AGL offers decimeter-level accuracy, making it suitable for robotics, unmanned vehicles, and asset tracking. Key aspects of the AGL system implementation are presented, emphasizing the importance of tight time-synchronization and addressing the impact of non-line-of-sight (NLOS) propagation. The main goal of this study is to validate the AGL system's performance, showcasing its efficacy through benchmarking studies. The results demonstrate the AGL system capability in delivering decimeter-level accuracy, even in dynamic and high multipath scenarios.

Keywords

Edge space, Multilitration, Time of arrival (ToA), Time Synchronization, Ultra-wideband (UWB)

1. Introduction

For positioning and tracking, many applications rely on the Global Navigation Satellite System (GNSS), commonly known as GPS, which on its own is a truly global and scalable system and works very well in the open spaces. However GNSS has limitations when it comes to operating in the edge spaces, such as inside buildings, tunnels, mines, onboard sea vessels oil rigs and wind-mil platforms, where the coverage may be unavailable, shaded, or the accuracy inadequate to support target applications. In this edge area, positioning accuracy down to couple of decimeters or better is needed, e.g., tracking and navigation of robotic devices in a warehouse, factory floor and autonomous take-off and landing of drones in a safe, reliable and efficient way from a ship in highly dynamic environment and challenging weather conditions. This provides motivation to invest research efforts to develop and realize innovative solutions that can work in areas with no, shaded or intermittent availability of GNSS signals, and thereby

Proceedings of the Work-in-Progress Papers at the 13th International Conference on Indoor Positioning and Indoor Navigation (IPIN-WiP 2023), September 25 - 28, 2023, Nuremberg, Germany

*Corresponding author.

Muhammad.Chaudhary@mil.be (M. H. Chaudhary); bart.scheers@mil.be (B. Scheers)

© 2023 Copyright for this paper by its authors. Use permitted under Creative Commons License Attribution 4.0 International (CC BY 4.0).

CEUR Workshop Proceedings (CEUR-WS.org)

CEUR-WS.org/Vol-3581/179_WiP.pdf

CEUR Workshop Proceedings ceur-ws.org ISSN 1613-0073

extend and expand the economic and societal benefits of the GPS like positioning service to the edge environments. The Agilica Geo-Location system (AGL) targets this kind of need.

The AGL is based on the Ultra-wideband (UWB) wireless access technology. The AGL can deliver accurate positioning down to 10 cm and is well-suited for robotics, unmanned vehicles in air or on ground and for asset tracking. The UWB technology uses low power and wide bandwidth signals that allow them to capture transmit and receive timing of the signals with fine resolution. The signals are robust to noise and interference. Based on the signal timing data and using a network of UWB anchor nodes and tags, positioning and tracking solutions can be developed for complex edge environments where other positioning technologies may struggle.

Compared to other navigation solutions such as based on ultrasonic sensors [1], radio frequency identification (RFID) [2], Inertial Measurement Units (IMUs), and visual systems [3, 4], UWB-based radio frequency navigation and tracking has advantages in environments that lack illumination or have low visibility, such as in the case of fog. Although, the acoustic based solutions can offer accuracy up to few centimeters but over a small coverage area, and their performance is sensitive to environmental factors such temperature, humidity, and acoustic noise. Commercially available MEMS based IMUs are often used for positioning and navigation of robotic devices, air and surface vehicles, often in combination with GNSS and vision based sensors. However, the IMU accuracy deteriorates with operation time. The vision based systems are often used in the drone and robotic sector, but the accuracy and reliability of these sensors are highly dependent on the prevailing weather and visibility conditions [5]. The UWB-based solutions are robust to electromagnetic noise and interference and immune to environmental factors such as acoustic noise, temperature, humidity, and visibility conditions. Additionally, UWB has the capability to provide accuracy down to sub-decimeter range which could be required to safely navigate robotic devices and UAVs in the edge spaces, ranging from navigation in indoor spaces to taking off and landing drones in maritime environments.

There are numerous UWB based positioning solutions proposed in the literature, but they have gaps in terms of robustness, scalability, flexibility and evaluation in realistic scenarios [6, 7]. A large majority are designed for asset tracking applications where position is calculated in a backend server. These solutions have scalability issues in terms of position update rate and tag density. As such these network-centric systems can be used for navigation applications with a feedback link from the server to the navigating device such as a UAV. This requires additional resources besides adding latency. Often these solutions are tested in environments where the impact of RF channel vagaries (multipath, interference and noise) is limited. In the edge space, such as on board ships, the metallic structure, confined spaces and narrow alleyways present extremely challenging propagation environment for RF signals. In such an operational environment, the existing solutions either do not work or fail to meet the requirements on the accuracy, and scalability in terms of number of users, spatial area coverage, and responsiveness [8, 9].

The AGL system offers a unified positioning system and methods that support both network-centric asset tracking and device-centric navigation applications simultaneously, all powered by the same anchor infrastructure [10]. This adaptability allows for the system to be easily customized to suit changing needs and deployment scenarios, making it both flexible and scalable. Thanks to a built-in auto-calibration mechanism, the system requires no manual calibration after installation. With intelligent signal processing algorithms designed to handle

complex RF channel vagaries, such as multipath, interference, and noise, the AGL system offers decimeter-range position accuracy even in challenging edge environments.

The AGL technology garnered recognition, leading to a patent application filed in January 2020 [10]. The AGL can support positioning of an unlimited number of tag devices in the device-centric mode without any impact on position update rate, mirroring the capabilities of GNSS/GPS technology. A milestone achievement occurred in September 2019 during the Smart City Wallonia exposition, where the AGL solution was successfully demonstrated in real-world settings, facilitating the precise positioning of autonomous shuttles within the indoor space [11]. The AGL solution represents the rebranded name for iPoint, which originates from a spinoff project funded by Innoviris Belgium. Its international presence was notably showcased at the Hannover Messe tradeshow in April 2021 [12]. Subsequently, similar UWB solutions have surfaced in the scientific literature, enabling GPS like device-centric positioning [13, 14].

This paper presents the AGL system and its key elements, with a particular focus on its effectiveness in real-world scenarios. To achieve the highly accurate positioning, tight time synchronization among anchors is crucial. The synchronization technique is presented in detail, along with an online mechanism to calibrate internal processing and antenna delays. The device-centric positioning engine, which relies on pseudorange measurements to the anchors, is also discussed, with a focus on identifying and mitigating various sources of error.

The main focus of this paper is to present and discuss the effectiveness of the AGL system with results from benchmarking studies conducted in real environments. Results of a synchronization scheme evaluated over a 4-hop anchor topology shows synchronization error under 0.2 ns measured in terms of the error standard deviation. This illustrates the potential spatial scalability that the AGL system can offer. The positioning accuracy is evaluated in static and kinematic scenarios. In the first scenario, the tag is static while in the second scenario the tag is mobile with average speed between 4 km/h to 7 km/h and maximum speed between 7 km/h and 11 km/h. In the static scenario, the median position error is around 10 cm, which increased to almost 15 cm in the dynamic scenario. The error values for the 95th percentile point are 15 cm and 25 cm, respectively for the static and dynamic scenarios.

2. System Description

As shown in Fig. 1, the AGL system comprises a number of spatially distributed anchor or beacon nodes deployed at known positions. The anchors are connected to a backend-server through Ethernet or WLAN link, and from the server the anchors can be configured and their performance monitored. The system supports positioning and tracking of two type of tag devices over the UWB channel. First type of tag is for device-centric positioning and navigation, and is attached to client-end device, such as a robot, drone, or human, that needs to know its position for navigation. The second type of tag is for network-centric track and trace application, and is attached to dumb assets for which a backend server or a management system needs to know their position, but not the asset itself.

In the device-centric positioning, an unlimited number of such tags can be simultaneously localized, with the position update rate independent of the tag density, just like the GPS receivers. However the AGL is not a replica of GPS system. There are some fundamental

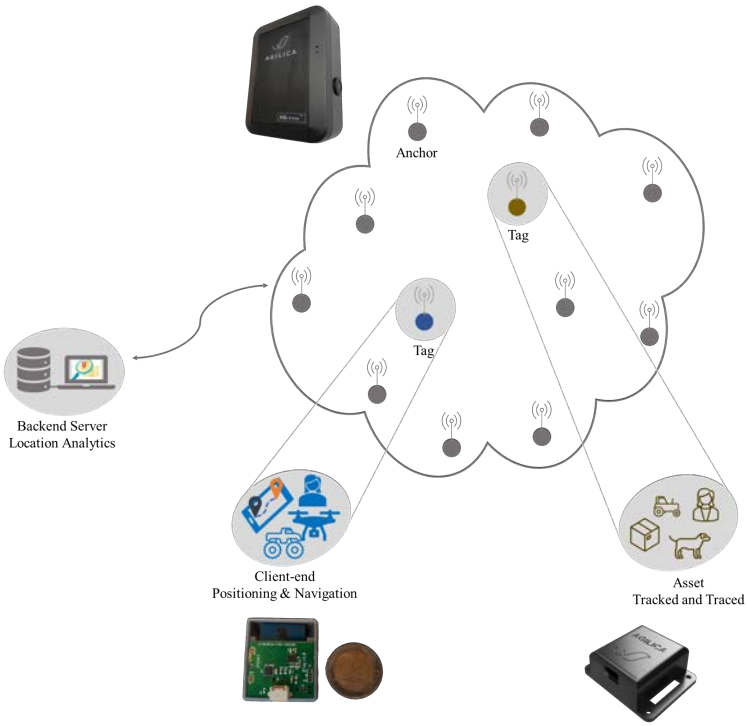

Figure 1: AGL system architecture.

differences. For instance, the GPS relies on atomic clocks in the satellites, whereas the AGL is using consumer grade crystal oscillators with stability in 10 to 20 ppm range. Each AGL anchor node periodically broadcasts navigation messages over the UWB channel. The anchors access the UWB channel using a TDMA-based medium access control. The structure of the TDMA frame can be configured through the backend server. The anchors and tags use these messages to synchronize their time. The accurate time synchronization is crucial to realize positioning of the tag devices. Synchronization accuracy within a few tens of micro-seconds is acceptable for the channel medium access control but for positioning of the tags, synchronization within a nanosecond or sub-nanosecond range must be achieved and maintained. As a reference, a nanosecond error in time synchronization corresponds to 30 cm error in distance. Thus highly accurate time synchronization scheme is needed for synchronizing the anchor network. The AGL system implements a multi-hop synchronization scheme over the UWB wireless channel. The multi-hop is needed to provide spatial scalability because the UWB is a low-power technology and the reliable communication range is quite limited. The ensuing Section 3 presents the details of this synchronization along with experimental results. Afterwards positioning method and performance results are presented in Section 4.

3. Time Synchronization

The common notion of time among the anchors can be achieved by sharing clock from a reference node. Due to limited communication range, clock has to be shared through sync

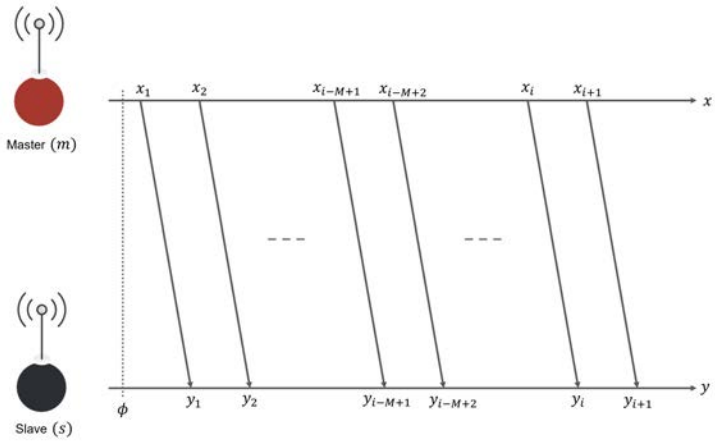

Figure 2: Clock sync model between master and slave nodes.

hierarchy comprising a tiered structure of reference nodes. We assume that each node has knowledge of its corresponding master node. In the ensuing discussion it suffices to focus on the interaction between a master–slave duo. The time synchronization scheme in the AGL system has two components which are implemented in a sequential and recursive way: (i) estimation and tracking of the clock parameters; (ii) estimation and compensation for the internal propagation delays on the sender and receiver side.

3.1. Clock Parameter Estimation

For clock parameter estimation, one of the schemes implemented in the AGL system is described in this section. Figure 2 illustrates the sharing of a clock between two nodes by exchanging time-stamped packets. The master node, denoted by m, serves as the reference node, while the node sharing its clock is referred as the slave node, denoted by s. Let x and y denote the time measured by the local clock at m and s, respectively. As depicted in Fig. 2, the master node periodically transmits packets at a specific interval. In the ith packet, the master node includes the transmit time-stamp x_i of the packet, while the corresponding receive time-stamp y_i is noted at the slave node. Based on practical clock characteristics such as phase difference denoted by ϕ, clock skew denoted by ω, and frequency drift between the two clocks denoted by $\mathscr{D}$, a precise relationship between the master and slave times can be modeled, as described in [15],

$$y_i = \phi + \omega x_i + \frac{1}{2}\mathscr{D} x_i^2 + \epsilon_i. \tag{1}$$

In equation (1), the observation noise affecting the measurement is represented by ϵ_i. It is assumed that either x_i or y_i is adjusted for the time-of-flight (ToF) of the packet, which can be calculated from the known positions of the anchors.

The clock parameters ϕ, ω, and $\mathscr{D}$ are known to vary over time due to the effects of temperature, component aging, vibration, and radiation on the clock circuitry [16]. However, in most cases these changes are slow enough to assume that they remain constant over a short time window. This allows to treat them as constant for the purpose of analyzing a batch of M measurements

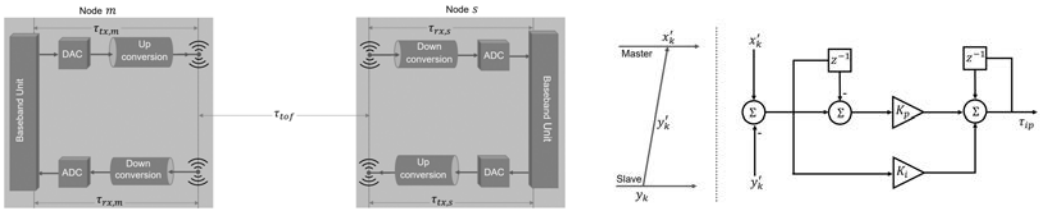

(a) Internal propagation delays.

(b) Outline of the PI control loop.

Figure 3: Radio transceivers internal propagation delays and control-loop.

within this window. Using these measurements, an estimate of the clock parameters can be obtained as

$$\hat{\theta} = (\mathbf{H}^T\mathbf{H})^{-1}\mathbf{H}^T\mathbf{y}, \quad \mathbf{C} = \sigma_\epsilon^2(\mathbf{H}^T\mathbf{H})^{-1}. \tag{2}$$

Here $\mathbf{C}$ denotes the error covariance of the estimator and

$$\theta \triangleq \begin{bmatrix} \phi \\ \omega \\ \mathscr{D} \end{bmatrix}, \quad \mathbf{y} \triangleq \begin{bmatrix} y_{i-M+1} \\ y_{i-M+2} \\ \vdots \\ y_i \end{bmatrix}, \quad \mathbf{H} \triangleq \begin{bmatrix} 1 & x_{i-M+1} & \frac{x_{i-M+1}^2}{2} \\ 1 & x_{i-M+2} & \frac{x_{i-M+2}^2}{2} \\ \vdots & \vdots & \vdots \\ 1 & x_i & \frac{x_i^2}{2} \end{bmatrix}.$$

The estimator in (2) assumes that the noise is zero mean with covariance $\mathbf{C} = \sigma_\epsilon^2\mathbf{I}$. The probability density function of the noise is otherwise unknown. In the absence of any knowledge about the observation noise, it can be shown that the above estimator is optimal in the least-squares sense [17, 18]

3.2. Internal Propagation Delay Estimation

In the context of time synchronization for the positioning and navigation systems, estimating and compensating clock parameters is not enough when it comes to building a positioning system with accuracy in some centimetre range. A key challenge is how to cope with propagation delays internal to the wireless communication devices, sometime also called transmit and receive antenna delays. These delays must be calibrated out as a part of the synchronization scheme.

As shown in Fig. 3a, the delay τ_{tx} on the transmit side denotes the time between the capturing of the transmit time-stamp of the packet to the time when the first sample of the packet leaves the transmit antenna. On the receive side, the delay τ_{rx} indicates the time when the first sample of the packet enters the receive antenna and the instance when the receive time-stamp is captured in the based-band processor. In [19, 20] typical values of these delays are discussed. These internal delays affect the time-stamp of the signals used for the positioning purpose and hence directly affect the positioning accuracy.

It is crucial to estimate and compensate the propagation delays internal to the clock master and the slaving device. In the AGL system, similar to the master, the slave node also transmits navigation packets on the UWB channel. In the kth packet, the transmit time-stamp translated

to the master clock is included, denoted as y'_k, see Fig. 3b. The corresponding receive time-stamp on the master x'_k is used in combination with the ToF τ_{tof} value (computed from the known positions of the two devices) to estimate the internal propagation delay. It can be shown that

$$\tau_{ip} \triangleq y'_k - x'_k - \tau_{tof} = \tau_{tx,m} + \tau_{rx,s} + \tau_{tx,s} + \tau_{rx,m}. \tag{3}$$

This computed value is feedback from node m to s in the next packet from m. The node s uses the classical proportional-integral (PI) control loop to track the this delay τ_{ip}. Fig.3b shows this loop filter. The output of this filter is the amount of time by which the transmit time-stamp y' of the next packet from s should be adjusted to compensate the internal delays.

3.3. Performance Evaluation

Using the above elements for estimation and tracking of clock parameters and internal propagation delays, we implemented a multi-hop synchronization scheme on a UWB test-bed using radio transceiver from Qorvo, compliant with IEEE 802.15.4-2011 standard [21]. We deployed five anchor nodes a_0 to a_4 as shown in Fig. 4a. Each node is driven by a low-cost XO as a clock source with stability on the order of +/-10 ppm. The anchor a_0 is designated as a grand-master and acted as the clock source. The clock is distributed to remaining nodes over wireless channel in a 4-hop synchronization topology. Node b is used as a test node that generated reference events by transmitting blink packets. All anchor nodes marked the receive time of these packets and forward them to a backend server. The time-stamps are adjusted by the corresponding distance between the node a_i and b. Then we computed the timing error between each anchor and the grand-master, and also with respect to its immediate clock master. The results are shown in Fig. 4b. We can see that the time synchronization error with respect to so called grand-master, measured in terms of standard deviation, remained below 0.2 ns (which corresponds to 6 cm distance) over the four hops.

4. Tag Positioning

In the self-positioning mode, the tag can compute and track its position based on the pseudorange measurements with respect to multiple AGL anchors, Fig. 5. For this position computation, there is well established array of signal processing tools and methods including variants of Kalman filtering.

These pseudoranges are estimated by the tag from the receive timestamp of the navigation packets broadcasted by the anchors, and the corresponding transmit timestamps. Since the transmission of these packets occurs sequentially in a TDMA frame, the tag clock drifts during this period. To ensure accurate positioning of the tag, it is essential to compensate for this drift. The AGL tag incorporates clock drift compensation mechanisms, based on a quadratic clock model in (1), which enable it to accurately estimate its position.

The pseudorange from the tag to an anchor can be expressed as shown in equation (4):

$$s_i = \underbrace{\sqrt{(x_t - x_i)^2 + (y_t - y_i)^2 + (z_t - z_i)^2}}_{\triangleq r_i} + \phi + \epsilon_i. \tag{4}$$

Here, s_i represents the pseudorange, r_i denotes the actual range, and ϕ is the offset between the anchor reference clock and the tag clock. The error in the range measurement, denoted by ϵ_i in

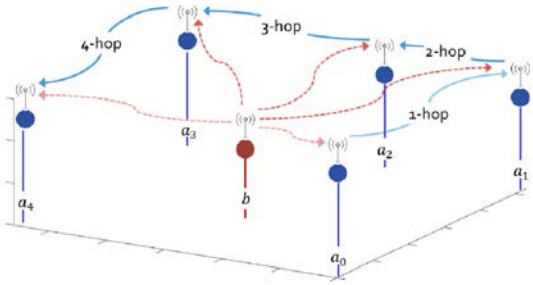

(a) Test setup comprising anchor nodes a_i and a test node b. Clock is distributed from node a_0 to remaining nodes over the wireless channel. The node b periodically sent blink messages. Sync error calculated based on receive time-stamp of these messages at anchor nodes.

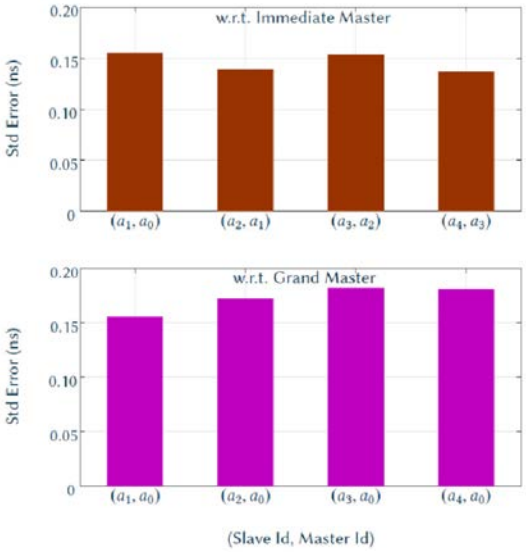

(b) Sync error statistics.

Figure 4: Test setup and results for the time synchronization.

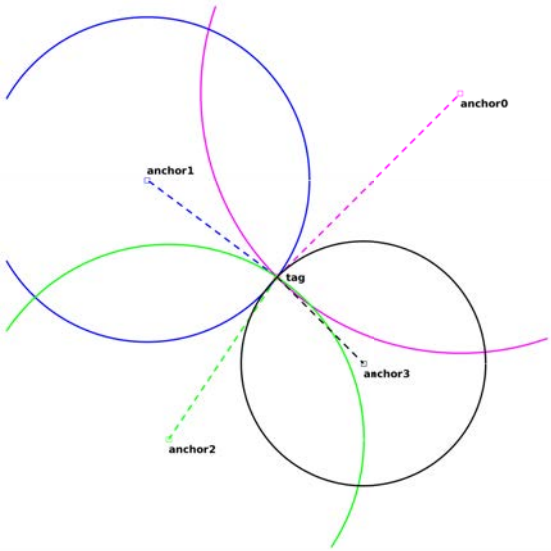

Figure 5: Tag positioning using the range measurements to multiple anchors for an ideal case of the noiseless measurements. In this case, all circles perfectly intersect at the tag position.

(4), is mainly caused by clock synchronization vagaries (ϵ_c), internal propagation delays (ϵ_d), and the impact of multipath and NLOS on the direct/first path detection (ϵ_m).

When computing the tag position, same error in the pseudoranges of the anchors does not have a significant impact on the accuracy. Most positioning algorithms can handle this type of error and it can be included as an additional unknown in the set of equations, lumped together with the offset term ϕ. However, it is crucial to minimize the variance in the error term ϵ_i across anchors. In the edge spaces, such as in a factory or onboard a ship, there could be a lot of metallic structures in close proximity causing heavy multipath and NLOS propagation. These wireless channel vagaries are the leading contributors to this variance. The accuracy and usefulness of a UWB positioning system depend on its ability to mitigate these impacts. To this end, the AGL tag implements a robust multi-layered multipath mitigation algorithm leveraging channel impulse response, receiver noise statistics and dynamics of pseudo ranges. The details of this algorithm will be published elsewhere in a separate publication. In the following sections, we present the performance evaluation of the AGL system in various test environments.

4.1. Performance Evaluation

To measure the accuracy of the positioning system, we define two types of errors: horizontal and vertical. The 2D horizontal error for a position estimate $(\hat{x},\ \hat{y})$ is defined as the distance between the estimated location of the tag reported by the positioning system and the actual position of the tag, i.e., $\epsilon_{h_i} = \sqrt{(\hat{x}_i - x_t)^2 + (\hat{y}_i - y_t)^2}$, where $(x_t,\ y_t)$ is the corresponding true position of the tag, also known as the *ground truth*. The cumulative distribution function (CDF) of the positioning error is defined as $\mathrm{CDF}(d) = \left(\epsilon_{h_i} < d\right)$. The vertical or height estimation error and corresponding CDF are defined as $\epsilon_{v_i} = |\hat{z}_i - z_t|$ and $\mathrm{CDF}(H) = \left(\epsilon_{v_i} < H\right)$, respectively. The root-mean squre (RMS) value for the horizontal and vertical errors are defined as

$$\epsilon_{h,} = \sqrt{\frac{1}{N}\sum_{i=1}^{N}\epsilon_{h_i}^2}, \quad \epsilon_{v,} = \sqrt{\frac{1}{N}\sum_{i=1}^{N}\epsilon_{v_i}^2}. \tag{5}$$

4.1.1. Indoor Sports-hall Tests—Static Scenario

The first set of tests were conducted in a sports-hall at Royal Military Academy Belgium. We evaluated the positioning accuracy in various system configurations. In this section, we present the results from one of the test configurations. Fig. 6a shows the test setup, where we deployed six anchors over an 18 m-by-9 m area. Among the six anchors, four were installed at a height of 3 m, while the remaining two were placed at a height of 0.25 m from the ground. We also tested the converse configuration and observed similar accuracy results.

To evaluate the accuracy of the AGL system, we set up a number of reference points within the anchor deployment area, as shown in Fig. 6b. At these test points, we logged the position estimates from the AGL tag and computed the empirical CDF for the 2D horizontal and vertical errors.

Fig. 7a displays the empirical CDF of the horizontal position error at test point $\mathbf{T_7}$. The figure highlights the RMS error value as well as the error at most commonly used reference points such as 50th, 68th and 95th percentile points.

Table 1 provides a summary of the horizontal error statistics for test points $\mathbf{T_0}$ to $\mathbf{T_{10}}$ in the sports hall setup. Notably, the worst-case error across all test points averages at 20 cm and the RMS error is approximately half of that. These results demonstrate the accuracy of the AGL

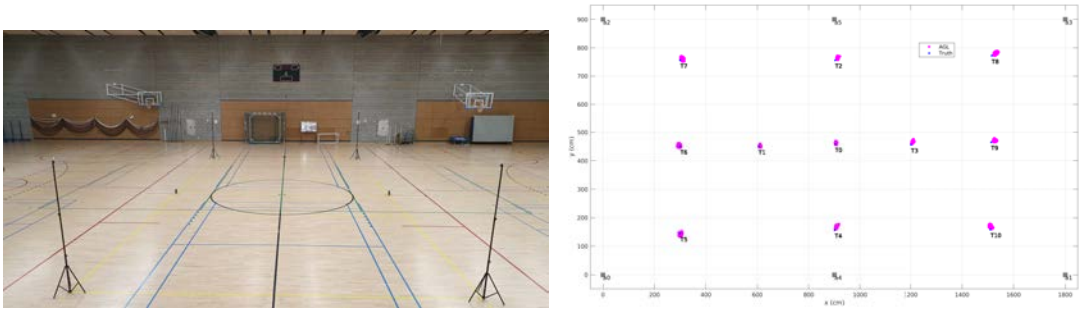

(a) Test setup in the sports-hall.

(b) Tag estimated and true positions at a number of test points within the anchor deployment area.

Figure 6: Sports-hall test.

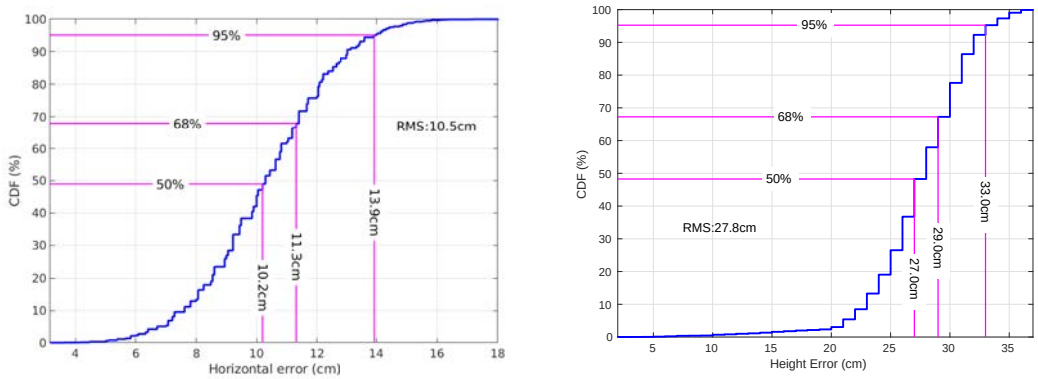

(a) Horizontal error CDF.

(b) Height error CDF.

Figure 7: Test point $\mathbf{T_7}$.

system and its consistency across multiple test points. The error variance that we see across the test points is mainly due to the geometric dilution of precision.

Fig. 7b shows the empirical CDF for the height error at test point $\mathbf{T_7}$. The summary statistics for the height error across all test points are presented in Table 2. On average, the worst-case error is limited to approximately 53 cm, the RMS error is slightly higher than half of this value, and the median error is approximately half of the maximum observed error. The vertical accuracy is contingent upon the deployment configuration and is not inherently constrained by the system itself. The accuracy in the vertical dimension can be further improved, for instance,by deploying more anchors and at three different heights instead of two.

4.1.2. Onboard Ship Testing—Static Scenario

We also conducted tests onboard a ship to access how well the AGL system is able to cope with the multipath in an environment with a lot of metallic structures in close proximity. We deployed six anchors on the ship deck, on easily reachable points, see Fig. 8. To gauge positioning accuracy, several test points were set up, and the average results across these reference points are tabulated in Table 3. Despite the challenging wireless conditions, we can

Table 1
Summary statistics for the horizontal error at the tests points.

Test Point	Position Error (cm)				
	RMS	**P_{50}**	**P_{68}**	**P_{95}**	**P_{100} (Max)**
T_0	7.6	7.2	8.1	10.6	13
T_1	7.1	7.0	7.6	9.2	12
T_2	13.1	12.8	13.9	16.4	24
T_3	14.0	13.9	14.8	17.2	22
T_4	12.5	12.0	13.0	15.8	27
T_5	4.7	4.0	5.2	7.8	11
T_6	5.7	5.2	6.4	9.1	14
T_7	10.5	10.2	11.3	13.9	18
T_8	18.5	17.9	19.7	24.2	30
T_9	15.7	15.3	16.5	19.7	24
T_{10}	11.1	10.4	12.0	15.2	21
Average	**10.9**	**10.5**	**11.7**	**14.5**	**19.6**

Table 2
The height estimation error statistics at the tests points.

Test Point	Height Error (cm)				
	RMS	**P_{50}**	**P_{68}**	**P_{95}**	**P_{100} (Max)**
T_0	33	32	33	35	38
T_1	23	22	23	26	41
T_2	27	27	28	31	33
T_3	11	10	12	14	17
T_4	13	11	13	15	63
T_5	20	19	21	26	31
T_6	54	53	55	59	64
T_7	28	27	29	33	37
T_8	22	20	23	26	40
T_9	52	49	51	57	70
T_{10}	23	23	25	28	32
Average	**27.8**	**26.6**	**28.5**	**31.8**	**52.5**

Table 3
The position error from the onboard ship testing.

	RMS	**P_{50}**	**P_{68}**	**P_{95}**	**P_{100} (Max)**
Average	**13.2**	**12.6**	**15.5**	**17.3**	**24.7**

Figure 8: Onboard ship testing setup.

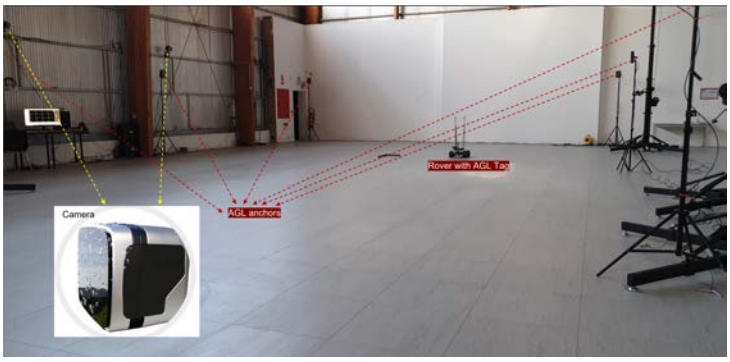

(a) Setup for benchmarking with motion capture system at ID2Move facility in Nivelles, Belgium.

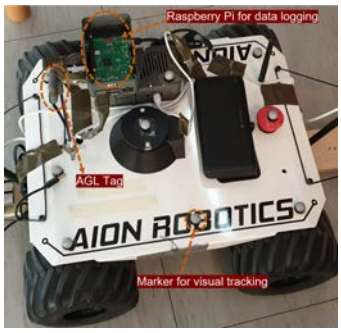

(b) Rover used in the motion capture benchmarking.

Figure 9: Test setup for benchmarking with visual motion capture system.

see that the AGL system demonstrated good accuracy, showcasing its resilience in such harsh environments.

4.1.3. Benchmarking Against a Visual Motion Capture System - Kinematic Scenario

The accuracy benchmarking with static test points has its limits because it does not capture and quantify the impact of dynamic scenarios where the tag is in motion. To address this gap, we conducted a benchmarking study using a visual motion capture system at one of the ID2Move test facilities in Nivelles, Belgium. The visual motion capture system is from Qualisys and consists of 12 cameras with 3 cameras installed on either side of a rectangular test zone. Fig. 9a shows two of these cameras in view. This Qualisys system can capture the exact position of the robotic devices with six degrees of freedom (6DOF) and in real-time with an accuracy better than a couple of centimeters. For this benchmarking study, we installed the AGL system comprising 6 anchors, shown in Fig. 9a. The tag was mounted on an unmanned ground vehicle (UGV). The UGV or rover is equipped with a Pixhawlk controller running Ardupilot software.

Fig. 9b illustrates the rover setup used in this benchmarking study. The setup included the AGL tag, several markers for visual tracking of the rover, and a Raspberry Pi for logging

Table 4
Rover speed in the test rounds.

Test Round	Speed (km/h)	
	Average	Max
$\mathbf{R_1}$	4.1	6.8
$\mathbf{R_2}$	5.2	8.6
$\mathbf{R_3}$	6.7	10.9

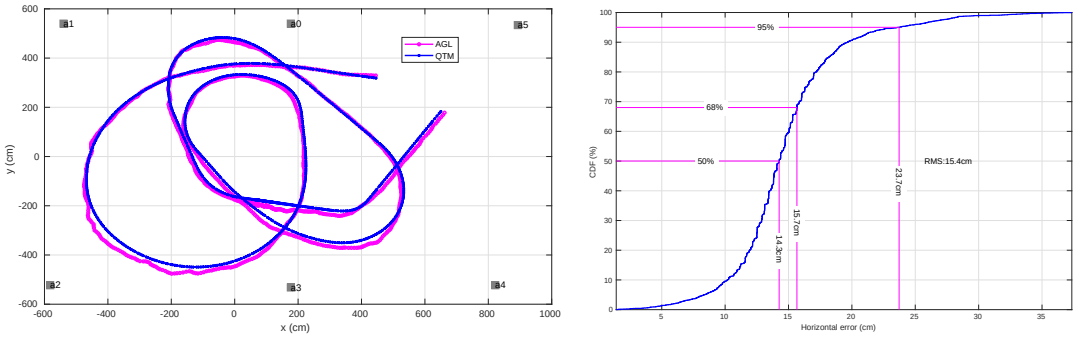

(a) Traversed path by the rover in $\mathbf{R_1}$ round from the AGL system and the QTM motion capture system.

(b) Horizontal error CDF in $\mathbf{R_1}$ round.

Figure 10: Results of round $\mathbf{R_1}$.

data from the AGL tag and the Qualisys Track Manager (QTM). All the cameras are connected to the QTM server where the 6DOF position is calculated. The server provides an SDK for streaming the position data in real-time over Ethernet or WiFi. We used the Raspberry Pi's WiFi connectivity to stream and log the position of the optical markers on the rover, as well as the position and orientation of the rover as a rigid body.

We conducted several rounds of tests with the rover, varying its speed and movement patterns. In the following sections, we present the results from three of these test rounds. Table 4 provides information on the average and maximum speed of the rover during these test runs.

To quantify the positioning accuracy of the AGL system, we used the position reported by the QTM server as the ground truth. We time-stamped, on the Raspberry Pi, the reception of data from both the AGL and QTM. For each AGL tag position data, we retrieved the corresponding data from the QTM log that was closest in time to the AGL time-stamp.

Fig. 10a shows the rover's path during round $\mathbf{R_1}$, with positions reported by both the AGL tag and the QTM system, as well as the positions of the AGL anchors labeled a_0 through a_5. Overall the two traces closely follow each other with slightly increased divergence towards the edges of the AGL deployment zone. This divergence is mainly due to the geometric dilution of precision inherent in such a positioning system. To quantify the positioning error, we plot the horizontal error CDF in Fig. 10b. The RMS error is 15.4 cm and the maximum error observed during this round is limited to 32 cm. The error at 50th, 68th and 95th percentile points on the CDF curve is 14.3, 15.7 and 23.7 cm, respectively. While these errors are slightly higher than those observed in the static scenario in the previous section, the accuracy is still quite good.

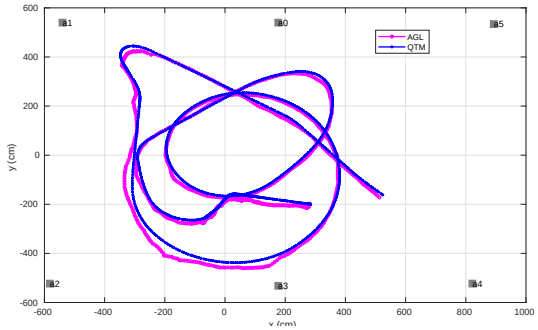

(a) Traversed path by the rover in $\mathbf{R_2}$ round from the AGL system and the QTM motion capture system.

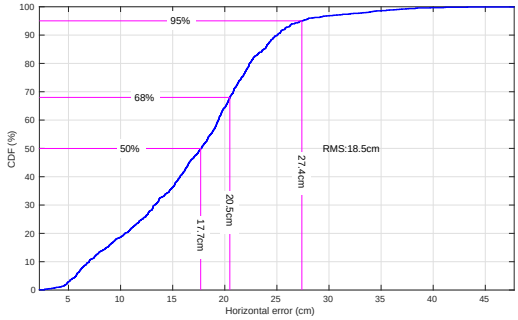

(b) Horizontal error CDF in $\mathbf{R_2}$ round.

Figure 11: Results of round $\mathbf{R_2}$.

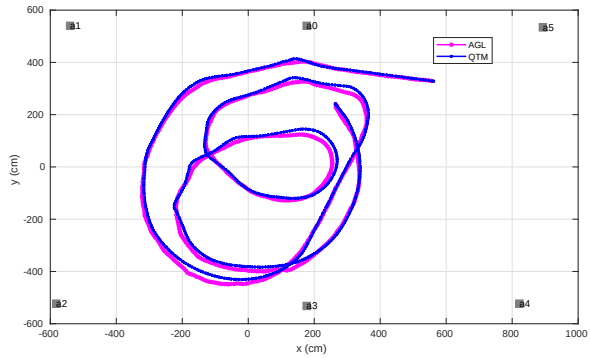

(a) Traversed path by the rover in $\mathbf{R_3}$ round from the AGL system and the QTM motion capture system.

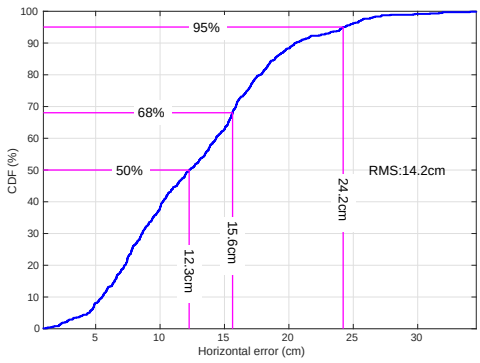

(b) Horizontal error CDF in $\mathbf{R_3}$ round.

Figure 12: Results of round $\mathbf{R_3}$.

Test round $\mathbf{R_2}$ results are presented in Figs. 11a and 11b, which show the path taken by the rover and the corresponding positioning error CDF, respectively. There is a slight increase in positioning error compared to round $\mathbf{R_1}$, which is reflected in the CDF in Fig. 11b. The error has increased on all percentile points but remains below 30 cm for almost 99% of the time. This increase can be attributed to both the higher speed of the rover during this round and the different path trajectory it followed. These choices were intentional in order to capture relevant accuracy degradation patterns.

The results for the test round $\mathbf{R_3}$ are shown in Fig. 12a and Fig. 12b. As shown in the first figure, the paths reported by the AGL tag and QTM system closely align with each other. In the second figure, the error CDF curve shows that the error remained below 30 cm for more than 99% of the time, and the RMS error was limited to 14.2 cm. It is noteworthy that, despite the highest speed of the rover in this run compared to the other two, the observed error is the lowest. This can be attributed to the fact that the rover traversed path remains relatively within the inner deployment zone of the anchors.

For easy referencing, Table 5 summarizes the results from this kinematic scenario.

Table 5
Summary statistics for the error during the test rounds.

Test Round	Speed (km/h)		Position Error (cm)				
	Average	Max	RMS	P_{50}	P_{68}	P_{95}	P_{100} (Max)
R_1	4.1	6.8	15.4	14.3	15.7	23.7	36.2
R_2	5.2	8.6	18.5	17.7	20.5	27.4	46.5
R_3	6.7	10.9	14.2	12.3	15.6	24.2	34.7
Average	**5.3**	**8.8**	**16.1**	**14.8**	**17.3**	**25.1**	**39.2**

5. Concluding Remarks

The work presented in this paper provides valuable insights into the accuracy and performance of the Agilica AGL positioning system. The test results show that the AGL system can provide decimeter level accuracy. In a static scenario, the position error at the 50th and 95th percentile points is around 10 cm and 15 cm, respectively. The error at these reference points respectively increased to about 15 cm and 25 cm, when the tag is moved with an average speed between 4 km/h to 7 km/h and maximum speed between 7 km/h and 11 km/h. This shows that the system can maintain high accuracy in kinematic scenarios where the tag is mobile.

The accuracy results have also been consistent across different test rounds, indicating the system reliability and robustness. The results also highlighted the impact of factors such as the reference point location, tag movement speed and trajectory on positioning accuracy, as well as the inherent limitations of the positioning system due to geometric dilution of precision. As such, it is important for users of such a positioning system to be aware of these factors and make appropriate choices in terms of deployment and usage to ensure optimal performance.

The paper has demonstrated the potential of the AGL system for accurate positioning in static as well as dynamic scenarios, while also highlighting the need for careful consideration of various factors that can impact accuracy, such as need for tight time synchronization, internal propagation delays compensation and the importance of minimizing the impact of multipath propagation. These results can be useful for researchers and practitioners in fields such as robotics, autonomous vehicles, and indoor positioning, where accurate and reliable positioning is essential for a range of applications.

The AGL system is built as an alternative and complementary to the GNSS for applications in the edge spaces that requires high accuracy and availability. However, it should be highlighted that when it comes to the alternatives to the GNSS, a single solution, technology or system cannot cater to the needs in all operational environments. It would be more feasible and sensible to create customized independent systems that are designed to function optimally within a particular environment or group of environments. However, these systems should have a standardized and compatible application interface so that data from multiple systems can be merged together when available to form a unified positioning system. The integrated system would be more robust, precise, and dependable. This approach underpins the AGL system.

References

[1] R. Kapoor, A. Gardi, R. Sabatini, Acoustic positioning and navigation system for GNSS denied/challenged environments, in: IEEE/ION PLANS Symposium, USA, 2020.

[2] A. Mortoni, A. Buffi, P. Nepa, A survey on indoor vehicle localization through RFID technology, IEEE J. Access 9 (2021) 17921–17942.

[3] S. Shen, N. Michael, V. Kumar, Autonomous multi-floor indoor navigation with a computationally constrained MAV, in: IEEE Int. ICRA Conf., China, 2021.

[4] A. Schutz et al., Precise positioning through a loosely-coupled sensor fusion of gnss-rtk, ins and lidar for autonomous driving, in: IEEE/ION PLANS Symposium, USA, 2020.

[5] Y. Alkendi, L. Seneviratne, Y. Zweiri, State of the art in vision-based localization techniques for autonomous navigation systems, IEEE J. Access 9 (2021) 76847–76874.

[6] M. Ridolfi, S. V. de Velde, H. Steendam, E. D. Poorter, Analysis of the scalability of UWB indoor localization solutions for high user densities, Sensors 18 (2018).

[7] J. Tiemann, C. Wietfeld, Scalability, real-time capabilities, and energy efficiency in ultra-wideband localization, IEEE Trans. Ind. Informatics 15 (2019) 6313–6321.

[8] K. Ishida, E. Okamoto, H.-B. Li, A robust indoor localization method for NLOS environments utilizing sensor subsets, IEEE Open Journal of Signal Processing 3 (2023) 450–463.

[9] F. Bonnin-Pascua, A. Ortiz, An UWB-based system for localization inside merchant vessels, in: 24th IEEE Int. ETFA Conf., Spain, 2019.

[10] M. H. Chaudhary, B. Scheers, Time-of-flight based unified positioning system and methods, 2020. EU Patent Filed 24 Jan., 2020.

[11] iPoint POC demonstration in Smart City Wallonia, Sept. 2019 in Marche-en-Fammene, Belgium, Last accessed on Aug. 4th, 2023. URL: https://youtu.be/qogFY8rWFFM.

[12] Agilica showcasing of AGL solution in Hannover Messe, April 2021, Last accessed on Aug. 4th, 2023. URL: https://www.hannovermesse.de/apollo/hannover_messe_2021/obs/Binary/A1089203/Agilica%20Taking%20GPS%20Further%20Article-compressed.pdf.

[13] L. Santoro et al., Scale up to infinity: the UWB indoor global positioning system, in: IEEE Int. ROSE Symposium, USA, 2021.

[14] L. Santoro et al., UWB-based indoor positioning system with infinite scalability, IEEE Trans. Instr. and Measur. 72 (2023).

[15] D. W. Allan, Time and frequency (time-domain) characterization, estimation, and prediction of precision clocks and oscillators, IEEE Trans. Ultrason., Ferroelect., Freq. Contr. 34 (1987).

[16] Handbook of frequency stability analysis, NIST Special Publication 1065, 2008.

[17] M. H. Chaudhary, B. Scheers, Practical one-way time synchronization schemes with experimental evaluation, in: IEEE Int. SPAWC Workshop, Greece, 2018.

[18] S. M. Kay, Fundamentals of Statistical Signal Processing: Estimation The., Pren.-Hall, 1993.

[19] M. H. Chaudhary, B. Scheers, Software-defined wireless communications and positioning device for IoT development, in: Int. ICMCIS Conf., Brussels, 2016.

[20] R. Lahouli, M. H. Chaudhary, S. Basak, B. Scheers, Tracking of rescue workers in harsh indoor and outdoor environments, in: 18th Int. AdHoc-Now Conf., Luxembourg, 2019.

[21] IEEE standard for local and metropolitan area networks part 15.4: Low-rate wireless personal area networks (LR-WPANs), IEEE Std. 802.15.4-2011, 2011.